A wind tunnel investigation of the effects of end and laminar/turbulent inflow conditions on cylinder vortex-induced vibrations

Rémi Bourguet, Romain Mathis

A wind tunnel investigation of the effects of end and laminar/turbulent inflow conditions on cylinder vortex-induced vibrations

Rémi Bourguet*, Romain Mathis

Institut de Mécanique des Fluides de Toulouse, Université de Toulouse and CNRS, Toulouse 31400, France

Abstract

The influence of end and inflow conditions on the vortex-induced vibrations of a cylinder is studied on the basis of wind tunnel experiments, combining measurements of the body displacement and flow velocity in its wake. The cylinder of length-to-diameter aspect ratio 5.5 has one end exposed to the current. It is elastically mounted in the cross-flow direction, with low damping. The structure to displaced fluid mass ratio is close to 1000. The behavior of the system is explored over a range of values of the reduced velocity, $U^\star$, defined as the inverse of the oscillator natural frequency, non-dimensionalized by the inflow velocity (U_∞) and the cylinder diameter (D), typically between 4 and 8, at a Reynolds number of the order of 10^4, based on U_∞ and D. Three end conditions are examined: two free-end conditions with either a flat or a hemispherical shape, and a condition where a fixed plate is placed close to the flat end. Three inflow states are considered: a laminar condition and two grid-generated turbulent conditions of different turbulence intensity levels (up to 10%) and comparable integral length scales, around 30% of D. Vibrations characterized by bell-shaped evolutions of their magnitude with $U^\star$ develop, under flow-body synchronization (lock-in), in all conditions, with peak amplitudes ranging from 4% to 12% of D. The free end causes a shift of the response bell-shaped curve towards higher $U^\star$ values. The shift may be such that there is no overlap between the vibration domains in the end-plate and free-end conditions. The passage from laminar to turbulent inflow conditions is found to attenuate this shift. A clear reduction of vibration amplitude is observed when the end plate is removed, and the amplitude is further reduced when the flat end is replaced by the hemispherical one. On the other hand, turbulent inflows induce a global enhancement of the vibration amplitudes, which may reach +45% relative to the laminar stream condition. The end/inflow conditions are also shown to impact the regularity of the structural responses.

Keywords: flow-structure interaction, vortex-induced vibrations, finite-length cylinder, free-end effects, laminar/turbulent freestreams, wind tunnel experiments

1. Introduction

Vortex-induced vibrations (VIV) of flexible or elastically mounted bodies with bluff cross-sections are ubiquitous in nature, e.g. oscillations of plants in wind or water streams, and are also common in civil, offshore and industrial engineering systems where they cause increased fatigue damage of the structures, such as heat exchanger tubes, cooling towers, spar hulls, risers or mooring lines. In the context of flow energy harvesting, these vibrations can also be employed as a mechanical energy converter. Due to their practical implications and their fundamental interest as a paradigm of fluid-structure interaction, VIV have motivated a number of research works, as reviewed, for example, by Williamson and Govardhan (2004), Sarpkaya (2004) and Païdoussis et al. (2010).

VIV have often been studied through the canonical problem of an elastically mounted, rigid circular cylinder, immersed in a uniform laminar current normal to its axis, and free to oscillate in the cross-flow direction (Feng, 1968;

*remi.bourguet@imft.fr

Mittal and Tezduyar, 1992; Khalak and Williamson, 1996; Hover et al., 1998; Shiels et al., 2001; Klamo et al., 2006; Leontini et al., 2006; Raghavan and Bernitsas, 2011; Riches and Morton, 2018; Konstantinidis et al., 2020). In this canonical problem, the cylinder end effects were generally suppressed or minimized, and a large length-to-diameter aspect ratio was usually considered so that further increase in cylinder length is not expected to change the system behavior. This idealized case, i.e. long cylinder without end effects, is referred to as infinite in the following. In such a configuration, VIV appear over a well-delimited range of values of the reduced velocity, $U^\star$, defined as the inverse of the oscillator natural frequency, non-dimensionalized by the inflow velocity and the cylinder diameter. Within this range, body motion and flow unsteadiness, associated with vortex formation in the wake, are synchronized. This mechanism of synchronization is referred to as lock-in. Under lock-in, the vibration frequency can deviate from the oscillator natural frequency, and the vortex shedding frequency can be driven away from that observed downstream of a stationary body (Strouhal frequency). VIV amplitudes exhibit bell-shaped evolutions as functions of $U^\star$. The width of the lock-in range, the associated deviations from the Strouhal and natural frequencies, and the maximum amplitude of vibration depend on the system parameters, in particular on the structural damping ratio and structure to displaced fluid mass ratio. The lock-in range and departure from the natural frequency tend to be smaller in air, where the mass ratio is usually large, than in water, for example. The maximum vibration amplitude, which may be larger than one diameter, globally follows a decreasing trend as a function of the product between the mass and damping ratios. This trend and, more generally, VIV properties, are also influenced by the Reynolds number, based on the inflow velocity and body diameter.

The cylinders encountered in practical applications are not infinite and may have one or both ends exposed to the current. This may modify the system behavior, compared to the above mentioned, idealized configuration. The present work explores the end effects experimentally, by considering an elastically mounted cylinder of low length-to-diameter aspect ratio, placed in a wind tunnel with one free end.

The impact of a free end on the flow dynamics and fluid forces has been well documented for stationary cylinders, especially for wall-mounted bodies (Farivar, 1981; Slaouti and Gerrard, 1981; Gerich and Eckelmann, 1982; Kawamura et al., 1984; Kareem et al., 1989; Zdravkovich et al., 1989; Fox and Apelt, 1993; Park and Lee, 2000; Schouveiler and Provansal, 2001; Kitagawa et al., 2002; Inoue and Sakuragi, 2008; Iungo et al., 2012; Sumner, 2013; Zhao and Cheng, 2014; Porteous et al., 2014). Several parameters such as cylinder aspect ratio or boundary layer thickness at the junction with the wall may modulate flow properties but persistent features related to the presence of the free end have been identified. The free end disrupts the organization of the von Kármán vortex pattern. Among other effects, it causes an inclination of the vortex rows relative to the cylinder axis, and the emergence of specific vortical structures near the end, such as symmetrical tip vortices. The frequency of flow unsteadiness is generally lower than for an infinite body and it often exhibits decreasing, stepwise or cellular trends towards the end. This results in a reduction of fluid forcing frequency, which suggests that the coincidence with the natural frequency would require higher $U^\star$ values once the body is free to vibrate, i.e. a shift of the lock-in range. Such phenomenon is actually observed, as discussed in the following. The effect of the end shape, for example flat versus hemispherical, on mean fluid forcing appears to become prominent for short cylinders, e.g. below an aspect ratio of 5 for a cylinder with two free ends in Zdravkovich et al. (1989). As illustrated by Park and Lee (2004) for a cylinder of aspect ratio equal to 6, a modification of the end shape may modulate the intensity of the tip vortical structures but it has only a limited impact on flow frequency content, even relatively close to the tip (3 diameters).

The question of the influence of the end condition has been less investigated for elastically mounted bodies. Morse et al. (2008) compared the VIV of a cylinder with an aspect ratio equal to 8 and a free end, to those observed when an end plate is placed close to the tip, thus attenuating the three-dimensional flow structures developing in this region. The peak amplitudes of vibration and global shapes of the responses were similar but the lock-in range occurred at slightly higher $U^\star$ in the former case. A comparable shift of the reduced velocity range was detected by Zhao and Cheng (2014) between infinite and truncated body configurations. The statistics of free-end cylinder VIV depend on the aspect ratio (Rahman and Thiagarajan, 2015; Azadeh-Ranjbar et al., 2018; Gonçalves et al., 2018a) but no general trend emerges from prior works. For very short cylinders (aspect ratio of 0.5), Gonçalves et al. (2018b) emphasized the influence of the end shape on floating body responses; this previous work considered the combined effects of the body shape and free surface, and the actual influence of the end shape on VIV still has to be analyzed independently. It should also be noted that most of the above mentioned studies focused on low mass ratios of the order of 1: they typically concern structural vibrations in water.

In the present work the impact of the end condition on VIV is examined for different inflow states, including

turbulent ones, as frequently encountered in practical applications. No consensus exists in the literature regarding the influence of free stream turbulence on VIV. As an example, comparable levels of turbulence intensity were found to either enhance (So et al., 2008) or reduce (Pastò, 2008; Trush et al., 2017) the structural responses. Such discrepancies may be explained by the number of parameters involved and their variations from one study to the other (e.g. aspect ratio, Reynolds number). Among these parameters, the role played by the turbulence integral length scale, at a given turbulence intensity level, may not be marginal, as suggested by prior works concerning stationary body wakes (Bearman and Morel, 1983; Basu, 1986). In particular, free stream turbulence is expected to alter the system behavior when its length scale is of the order of the cylinder diameter; this point is taken into account in the present work. Concerning more specifically free-end effects, the reduction of flow unsteadiness frequency and its distribution along the span seem to persist for stationary cylinders immersed in turbulent streams (e.g. Basu, 1986; Kareem et al., 1989). The effect of rounded end shapes on the reorganization of the tip vortices (in the form of vortex archs) also appears to be robust towards substantial variations in turbulence intensity (Hajimirzaie et al., 2012). The robustness of the end effects under turbulent inflows needs to be assessed in the vibrating body case.

This brief review shows that several facets of end and inflow condition effects on VIV remain to be clarified, especially for large mass ratios. An attempt to shed some light on these aspects is proposed here on the basis of wind tunnel experiments. A rigid cylinder of aspect ratio 5.5 and mass ratio close to 1000 is elastically mounted in the cross-flow direction, with low structural damping, and its VIV are examined over a range of reduced velocity values, at a Reynolds number of the order of 10^4. Three end conditions are considered: two free-end conditions with either a flat or a rounded shape, and a condition where a fixed plate is placed close to the flat end, as in Morse et al. (2008). The impact of these end conditions on the flow-structure system behavior is investigated for three distinct inflow states, a laminar stream, and two grid-generated turbulent streams of different turbulence intensity levels (up to approximately 10%) and integral length scales commensurable to the body diameter. The paper is organized as follows. The physical system and the experimental method are presented in §2. As a first step, in §3, focus is placed on the flow dynamics downstream of the fixed cylinder. The VIV of the elastically mounted body are examined in §4. The main findings of this work are summarized in §5.

2. Physical system and experimental method

The experiments are carried out in the closed-circuit wind tunnel S2 of the Institut de Mécanique des Fluides de Toulouse (IMFT). The wind tunnel has a test section of 1.8 m × 0.5 m × 0.5 m and can be equipped with different grid arrangements in order to achieve specific turbulent inflow conditions, as shown hereafter. The characteristics of the mechanical oscillator installed in the wind tunnel are described in §2.1. The inflow condition properties and flow measurement techniques are presented in §2.2. The procedure adopted to conduct the fixed and elastically mounted body tests is explained in §2.3.

2.1. One-degree-of-freedom oscillator

A sketch of the experimental setup is presented in figure 1(a). The cylinder is rigid, has a circular cross-section and a smooth surface. Its main part is made of carbon fiber tubing and different ends have been printed of ABS plastic. Its diameter, D, is equal to 60.3 mm. It is immersed in the test section through the roof of the wind tunnel so that its lower end is exposed to the flow. The lateral blockage ratio, i.e. ratio between the cylinder diameter and test section width, is close to 12%, which was shown to be low enough to limit the influence of the walls (e.g. Govardhan and Williamson, 2006). The body length immersed in the test section, L, is equal to 332 mm, giving an aspect ratio $L/D = 5.5$. A low aspect ratio was selected because the influence of the free end is expected to be more significant than for longer bodies. It is also representative of many engineering applications, e.g. chimney stacks, buildings. The free end is located at 168 mm from the test section floor, far from the boundary layer developing on this surface (this aspect is addressed in the next subsection).

The three end conditions studied in this work are schematized in figure 1(b). Two free-end conditions are considered, where the end of the cylinder is either flat or hemispherical; they are referred to as the FF (free flat) and FH (free hemispherical) end conditions in the following. The third condition, where a thin plate is placed close to the flat end, is referred to as the EP (end plate) condition. In the EP condition, the square end plate of 15 cm × 15 cm × 2 mm is rigidly mounted on the floor of the test section and positioned at 1 mm approximately below the cylinder end. It has

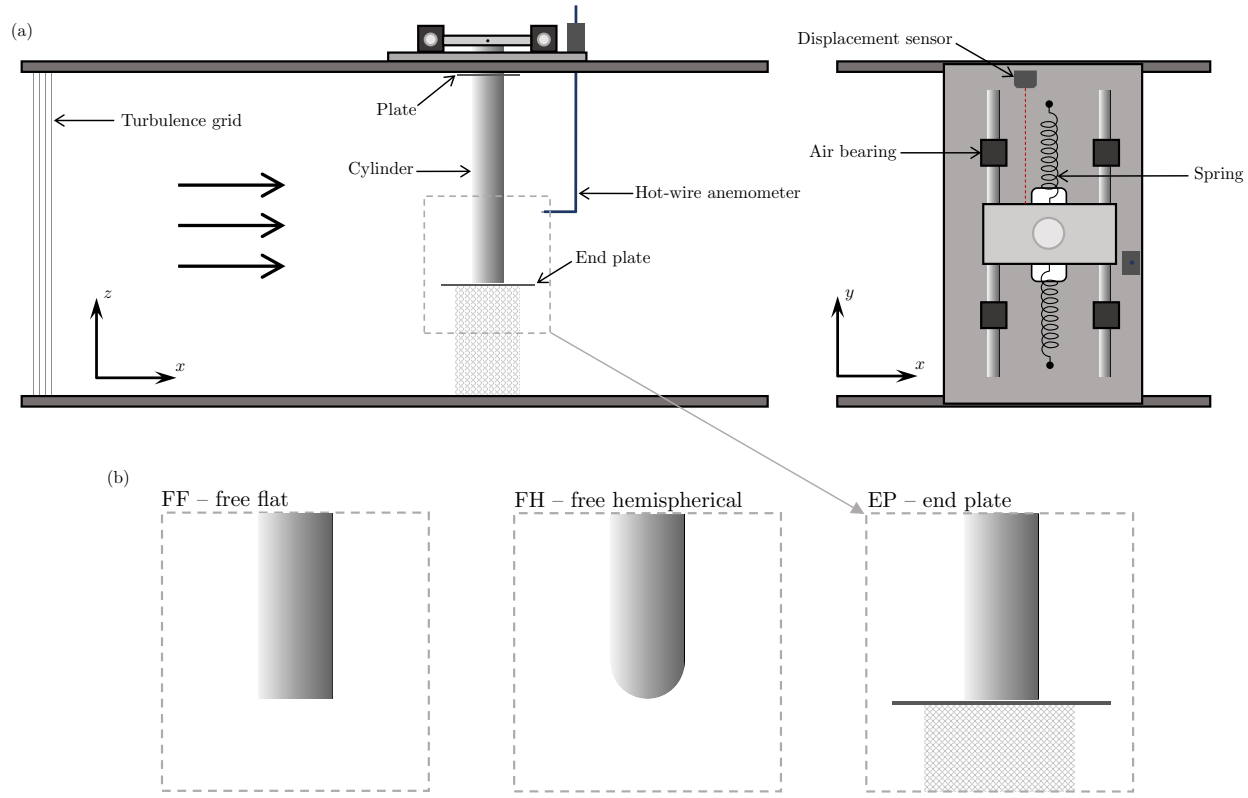

Figure 1: Schematics of the (a) experimental setup (side and top views) and (b) cylinder end conditions.

been verified that modifying the shape of the end plate (from square to circular) and slightly varying its distance from the tip (up to 3 mm and thus keeping the gap lower than $0.15D$, as suggested by Morse et al. (2008)) do not change the structural responses.

The cylinder is attached, through a groove pierced in the test section roof, to a carriage mounted on low-damping air bearings in the cross-flow direction (y axis), thus with a single degree of freedom, and connected to a fixed housing by linear springs. For the fixed body tests, the carriage can be locked to suppress the degree of freedom. A rectangular plate of 10 cm $\times$ 15 cm $\times$ 1 mm is attached to the cylinder at 1 mm approximately from the groove, in order to minimize flow deviation/leakage through the roof.

The displacement of the cylinder, ζ, is recorded using a non-contacting laser sensor (Keyence LK-G407; maximum sampling frequency and resolution of 50 kHz and 2 μm, respectively), aligned with the direction of motion as shown in figure 1(a).

The moving mass of the oscillator is kept constant for the different end conditions, m_s = 995 g. The mass ratio based on the volume of the cylinder immersed in the test section (V_s), $m^\star = m_s/(\rho V_s)$, where ρ is the air density (ρ = 1.2 kg/m^3), is equal to 875 and 903 for the flat (FF and EP conditions) and hemispherical (FH condition) ends, respectively. The natural frequency (f_n) and damping ratio (ξ) of the oscillator have been determined via free-decay tests, by giving the body an initial displacement and then recording its oscillations over 120 s. An example is depicted in figure 2 for the FF end condition (t designates the time variable). The natural frequency is obtained by fast Fourier transform (FFT) of the displacement time series. The damping ratio is issued from an exponential fit of the displacement signal envelope (black line in figure 2). The tests have been repeated several times with different initial displacements, for each end condition. They showed no significant variation of the natural frequency and damping ratio, including between the different end conditions. The averaged values based on all tests are f_n = 8.73 Hz and ξ = 0.0011, with small standard deviations equal to 0.01 Hz and lower than 10^{-4}, respectively.

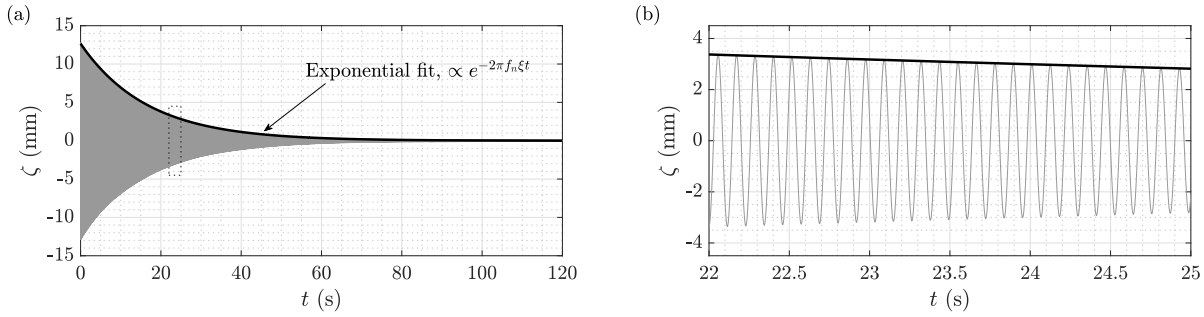

Figure 2: Time series of the cylinder displacement during a free-decay test (FF condition): (a) entire time series and (b) selected time interval (dotted rectangle in (a)). A black line denotes the exponential fit employed to determine the structural damping ratio.

2.2. Flow conditions and measurement

The inflow velocity, denoted by U_∞, is measured by a Pitot-static tube (Furness FCO318 pressure transducer) at mid-height of the cylinder test plane, $2D$ aside from the cylinder centerline. A closed-loop control procedure is employed to keep the inflow velocity constant. During the present tests, U_∞ is varied from 2.25 to 4.25 m/s.

Three inflow conditions are achieved by considering the empty wind tunnel, whose turbulence intensity is low, and by placing grids at the inlet of the test section. Two grids composed of square-mesh arrays of rectangular bars are employed. Such grids are expected to generate nearly isotropic turbulence, with low Reynolds number dependence (Roach, 1987). The distance between the bars is $g = 26$ (52) mm, and the bars are $d = 4$ (8) mm wide and 8 mm thick for grid 1 (grid 2, respectively). The porosity of both grids is the same, $\beta = [1 - d/(g + d)]^2 = 0.75$. The position of the cylinder in the test section, 545 mm from the inlet where the grids are installed, which represents 18.2 $(g + d)$ and 9.1 $(g + d)$ for grid 1 and grid 2, respectively, has been chosen to ensure a significant level of turbulence intensity as well as its homogenization, i.e. the traces of grid geometry have vanished (Cardesa et al., 2012). The three inflow conditions are referred to as NG (no grid), G1 (grid 1) and G2 (grid 2) in the following.

Each inflow condition is characterized by means of hot-wire anemometry at the streamwise position where the cylinder is immersed in the test section. A miniature single wire probe is used. It consists of a 5 μm-diameter and 1.25 mm long tungsten wire (DANTEC-55P11), operated by an A. A. Labs AN-1003 anemometer. The sampling frequency is set to 2 kHz. The wire sensor is mounted on an vertical Isel traverse system (LES 4 slide driven by an IMC-S8 controller). This anemometry technique is also employed to quantify flow unsteadiness downstream of the cylinder, as explained in §2.3. The time series of flow velocity (u) collected via hot-wire anemometry over 240 s are used to determine locally the mean flow velocity, $\overline{u}$ where $\overline{\ }$ represents the time-averaging operator, the turbulence intensity, $I_u = u'/U_\infty$ where $'$ denotes the root-mean-square (RMS) value of the fluctuation $(u-\overline{u})$, and the turbulence integral length scale, L_u. The integral length scale is quantified via the integration of the normalized auto-correlation down to a threshold of 0.1, instead of the first zero crossing, as the low-frequency energy content generated by the grids prevents the auto-correlation from reaching zero (e.g. Dogan et al., 2016; Trush et al., 2020). The approach based on a fit of the von Kármán velocity-spectrum model (Dyrbye and Hansen, 1997) leads to comparable values.

The mean values and standard deviations of I_u and L_u at the center of the test section, for $U_\infty \in [2.25, 4.25]$ m/s, are reported in table 1. No value is reported for L_u in the NG condition considering the low level of turbulence intensity. For each condition, the turbulence properties exhibit relatively small dispersion over the inflow velocity range under study. The spatial uniformity of flow properties in the plane where the tests are conducted has also been verified: excluding the near-wall regions where boundary layers develop, the standard deviations of $\overline{u}$, I_u and L_u across the test plane at fixed U_∞ are small, for example 0.02 m/s, 0.2% and 1.2 mm at $U_\infty = 2.8$ m/s, in the G1 condition. Concerning boundary layer thickness, in the parameter space investigated, the threshold $\overline{u} = 0.95U_\infty$ is always reached within the first 50 mm ($0.8D$) from the wall. Therefore, the region of large velocity gradients is limited to a short portion of the cylinder span in all cases, and most of the body is exposed to a current that is essentially uniform.

To summarize, in the NG condition, the oncoming flow is close to laminar and is referred to as laminar in the following. Grids 1 and 2 induce substantial turbulence intensity levels around 6% and 10%, respectively, with comparable integral length scales of the order of 30% of the cylinder diameter.

Table 1: Inflow condition properties at the streamwise position where the tests are conducted. The mean values and standard deviations (in square brackets) have been determined for $U_\infty \in [2.25, 4.25]$ m/s, i.e. the inflow velocity range investigated.

Inflow condition	Turbulence intensity, I_u (%)	Integral length scale, L_u (mm)
No grid, NG	0.6 [< 0.1]	–
Grid 1, G1	6.3 [0.6]	17.6 [0.5]
Grid 2, G2	9.7 [0.2]	18.4 [0.6]

2.3. Test procedure

A total of nine distinct conditions are examined in this work, three end conditions (FF, FH and EP) and three inflow conditions (NG, G1 and G2). They are designated by combining the end and inflow condition names as follows, FF-NG, EP-G1, etc. For each condition, two series of tests are performed, first with the rigidly mounted cylinder and then with the elastically mounted cylinder.

In the fixed body tests, the above described hot-wire anemometry technique is employed to quantify the intensity and frequency content of flow unsteadiness downstream of the cylinder. The measurements are conducted along the span with a resolution of $0.25D$, at a constant horizontal position, $3.5D$ downstream and $0.75D$ aside from the cylinder centerline. Each measurement is carried out over 240 s.

In the elastically mounted body tests, the hot-wire anemometry at a fixed spanwise position in the wake ($1.5D$ from the test section roof) is synchronized with the measurement of the cylinder displacement by the non-contacting laser sensor. The inflow velocity range corresponds to values of the reduced velocity, $U^\star = U_\infty/(f_n D)$, varying from 4.27 to 8.07. The corresponding Reynolds number based on the cylinder diameter, $\mathrm{Re} = \rho U_\infty D/\mu$ where μ designates the air viscosity ($\mu = 1.8 \times 10^{-5}$ Pa s), ranges from 9×10^3 to 17×10^3. The tests have been automated as follows. For each condition, the inflow velocity is set to the lowest value of the predefined range, the measurements start after 120 s so that the flow-structure system can reach a permanent state, data are collected over 240 s and stored, and the inflow velocity is then set to the next predefined value, etc. Prior works concerning VIV have shown that the system may exhibit hysteretic behaviors (e.g. Klamo et al., 2006; Prasanth et al., 2011). Such behaviors have indeed been detected over narrow $U^\star$ ranges at the edge of the vibration regions by repeating some tests with decreasing velocities. However, the principal trends reported in this paper appear to persist regardless of the initial conditions. The hysteresis phenomenon is not further investigated in the present work. For selected cases, hot-wire measurements are also carried out along the span, following the same procedure as in the fixed body tests, in order to quantify the alteration of the wake dynamics once the body oscillates.

The frequency spectra of the flow velocity and body response are obtained via FFT of the collected time series. The displacement signal is centered in all studied cases, i.e. $\overline{\zeta} = 0$. As noted by Riches and Morton (2018), several approaches are employed in the literature to quantify the vibration amplitudes. The maximum value of the displacement signal may be too sensitive to rare events encountered in turbulent flows, while the RMS value of the displacement signal may mask envelope modulations. The average of the top 10% of the displacement peaks (e.g. Hover et al., 1998) is adopted here and denoted by ζ_{10}. The use of other statistics, for comparison purpose with prior works, is explicitely stated. The successive peaks of the displacement signal define its envelope, σ. The RMS value of the envelope fluctuation (σ') is employed to measure the regularity of the structural vibrations. In the presentation of the results, the physical quantities are generally non-dimensionalized by D and U_∞.

3. Flow unsteadiness downstream of the fixed body

The intensity of flow unsteadiness downstream of the rigidly mounted cylinder and its evolution along the span are visualized in figure 3 through the RMS value of flow velocity fluctuation non-dimensionalized by the freestream velocity, for the nine end/inflow conditions. The results reported in this figure have been obtained for $U_\infty = 3$ m/s (which corresponds to $U^\star = 5.7$) but the profiles of u'/U_∞ are similar over the velocity range under study ($U_\infty \in [2.25, 4.25]$ m/s).

In the EP condition, the intensity of flow unsteadiness remains relatively uniform along the span and its level is comparable for all inflow conditions. The small spanwise modulations may be explained by the asymmetry of

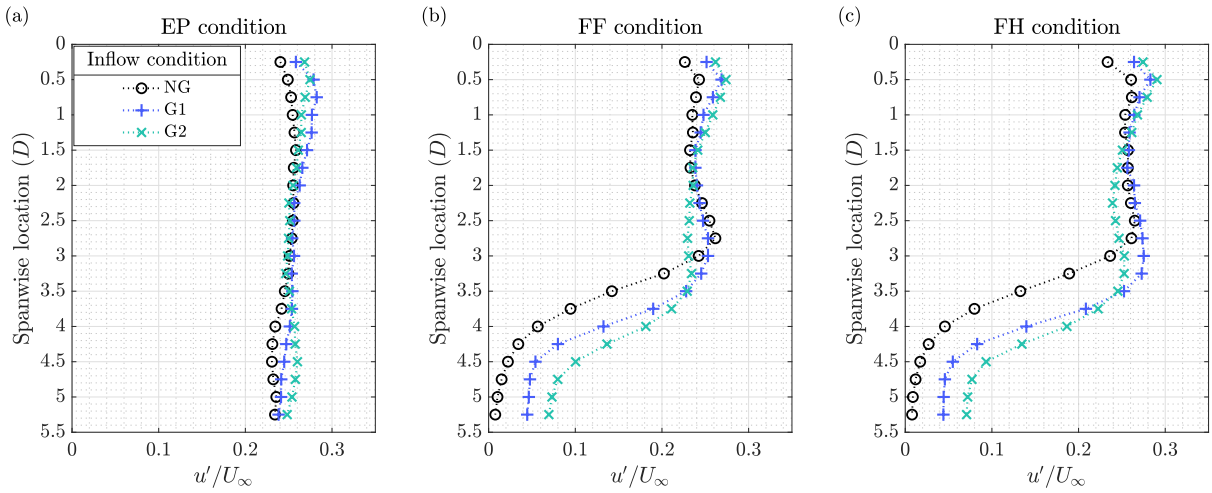

Figure 3: Spanwise evolution of the RMS value of flow velocity fluctuation in the wake of the fixed cylinder ($3.5D$ downstream and $0.75D$ aside from the centerline), in the (a) EP, (b) FF and (c) FH end conditions, for each inflow condition and $U_\infty = 3$ m/s ($U^\star = 5.7$). The RMS values are non-dimensionalized by the freestream velocity. Along the span, $0D$ corresponds to the cylinder base (test section roof) and $5.5D$ to its tip.

the end conditions, i.e. end plate versus test section wall. In particular, the boundary layer developing on the latter surface is thicker. A slight inflection of the profiles can be noted close to the test section wall; it appears in all studied conditions. In the free-end conditions (FF and FH), a region of uniform intensity persists downstream of the upper part of the cylinder, with levels comparable to those observed in the EP condition. A drop of flow unsteadiness intensity occurs downstream of the lower part of the body. The intensity levels measured near the free end are close to those of the freestream at this streamwise location of the test section ($3.5D$ downstream of the test plane). Such a drop illustrates how the presence of the free end can contaminate the wake, away from the cylinder tip. This phenomenon has been extensively documented in prior studies (e.g. Sumner, 2013). Two elements can be noted here. First, no substantial effect of the end shape (FF versus FH) emerges from the unsteadiness intensity profiles. Second, the intensity drop tends to occur closer to the free end under turbulent inflow conditions than in the laminar condition: beyond $3.25D$ from the base in the G1 and G2 conditions, versus $2.75D$ in the NG condition. This suggests that the contamination of the wake could be slightly reduced by freestream turbulence.

The frequency content of the wake is depicted in figure 4. At each spanwise location, the spectral amplitude of flow velocity fluctuation is normalized by its maximum value and the frequency range (f designates the frequency variable) is non-dimensionalized by D and U_∞. As in figure 3, the results are plotted for $U_\infty = 3$ m/s but they are representative of the typical features encountered across the velocity range investigated.

A single frequency, close to constant along the span, dominates the wake in the EP condition, regardless of the inflow condition. Some secondary spectral contributions are observed close to the end plate. They tend to vanish as the freestream turbulence level is increased. The span-averaged value of the dominant, non-dimensional frequency, is used to determine the Strouhal frequency (St). It is specified in each panel and visualized by a gray dashed line in the spectra. In the NG condition, the Strouhal frequency is equal to 0.194 and thus comparable to the values reported in laminar streams in the same Reynolds number range (here $\mathrm{Re} = 12 \times 10^3$), for cylinders of large aspect ratios without free ends, i.e. infinite bodies (Norberg, 1994). Turbulent inflows result in a slight increase of St, as also noted in previous works (e.g. Surry, 1972; Blackburn and Melbourne, 1996; Pastò, 2008), up to 0.2 in the G2 condition. The presence of the free end disrupts the frequency content of the wake. A spanwise cell dominated by a relatively constant frequency can still be observed on the base side, but several less-organized spectral contributions, mainly at lower frequencies, arise along the rest of the span. The averaged value of the dominant frequency along the upper third of the span (up to $1.75D$) is employed to define the Strouhal frequency in the free-end conditions (gray dashed line in each plot). The values of St are considerably reduced compared to the EP condition, for example St = 0.14 in the FF-NG condition. Such a reduction and comparable St values were reported in prior studies concerning similar configurations, as reviewed by Porteous et al. (2014). As previously noted for the unsteadiness intensity level, no

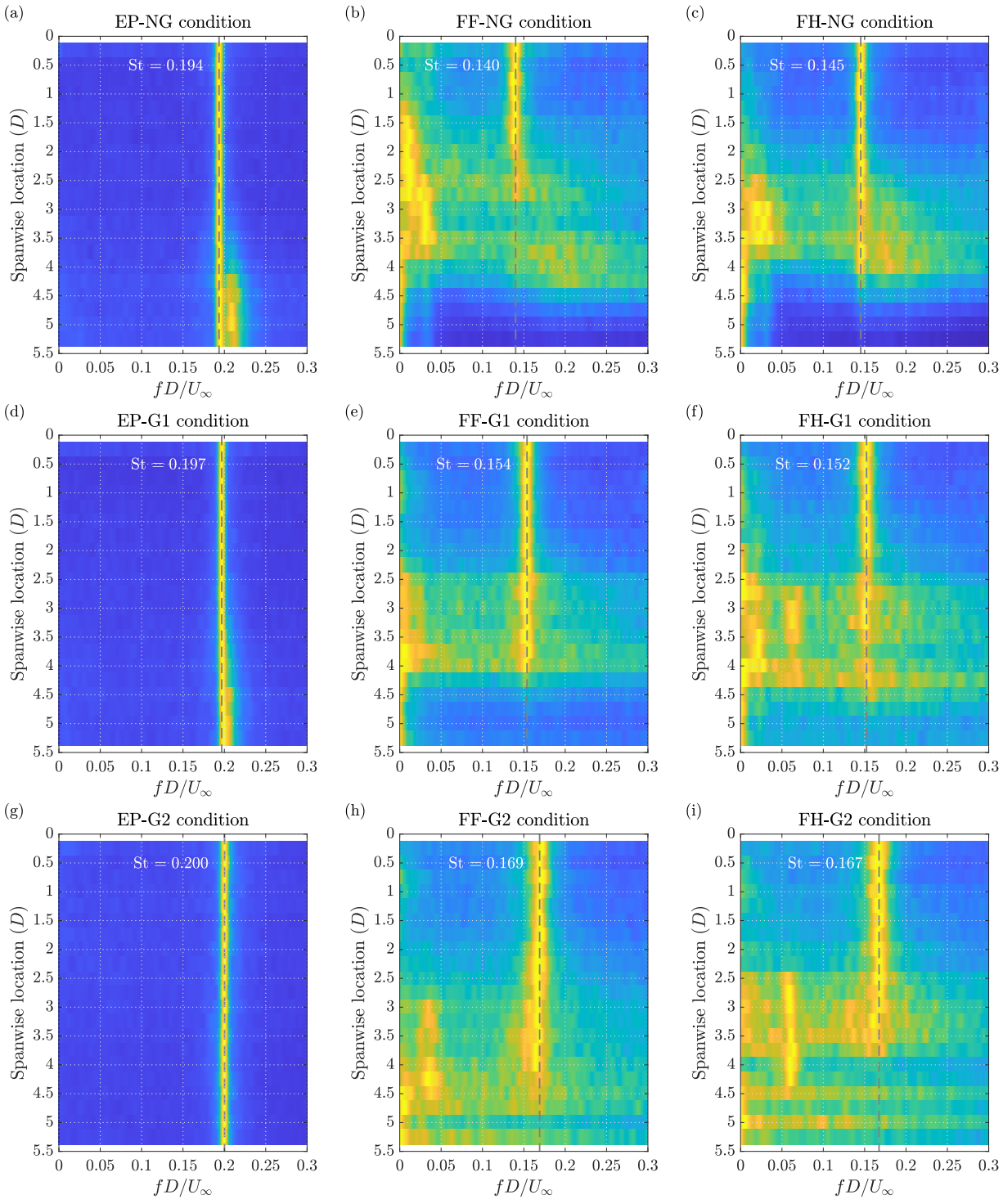

Figure 4: Spanwise evolution of the frequency spectrum of flow velocity fluctuation in the wake of the fixed cylinder (3.5D downstream and 0.75D aside from the centerline), in the (a) EP-NG, (b) FF-NG, (c) FH-NG, (d) EP-G1, (e) FF-G1, (f) FH-G1, (g) EP-G2, (h) FF-G2 and (i) FH-G2 conditions, for U_∞ = 3 m/s ($U^\star$ = 5.7). Along the span, 0D corresponds to the cylinder base (test section roof) and 5.5D to its tip. The spectral amplitude is normalized by its maximum value at each spanwise location and the color levels range from 0 (blue) to 1 (yellow). The frequency range is non-dimensionalized by the body diameter and freestream velocity. A gray dashed line represents the Strouhal frequency determined based on the value of the dominant frequency averaged over the entire span in the EP condition, and over its upper third in the FF and FH conditions; the value of St is indicated in each panel.

clear influence of the end shape can be identified. The increasing trend of St under the effect of freestream turbulence is found to persist and is even more pronounced in the free-end conditions. The maximum value of St, 0.169 in the FF-G2 condition, remains however lower than in the EP condition. It should be mentioned that the nine values of St reported in figure 4 are close to constant over the Re range investigated in the present study; this point is further discussed in §4.2.

On the basis of these observations concerning flow unsteadiness downstream of the fixed cylinder, three main trends may be hypothesized regarding VIV properties, once the body is elastically mounted. First, assuming that VIV occur close to $U^\star = 1/\mathrm{St}$, the reduction of St in the free-end conditions is expected to induce a shift of the VIV responses towards higher $U^\star$ values, compared to the EP condition. Second, freestream turbulence is expected to have the opposite effect, especially for the free-end conditions, and thus it could attenuate the shift of the $U^\star$ range relative to the EP condition. Third, no major effect of the end shape is expected. These conjectures are examined in the next section.

4. Vortex-induced vibrations

The behavior of the flow-structure system is investigated in this section through combined measurements of the body responses and wake dynamics. The reference condition where the cylinder is immersed in a laminar stream without free end, is considered as a first step, in §4.1, which includes a comparison with data reported in previous experimental studies. The alteration of the system behavior in the different end/inflow conditions is explored in §4.2.

4.1. Structural response in the reference condition (EP-NG) and comparison with prior works

The vibration amplitude in the EP-NG condition is represented as a function of the reduced velocity in figure 5, through the maximum (panel (a)) and RMS (panel (b)) values of the displacement signal, non-dimensionalized by the cylinder diameter. The response amplitude exhibits a bell-shaped evolution, typical of VIV, with a peak value close to 8% of D. The largest amplitudes are encountered close to the value of $U^\star$ that corresponds to the coincidence between the natural frequency of the oscillator and the Strouhal frequency identified in §3, $U^\star = 1/\mathrm{St} = 5.15$. The bell-shaped curve is however not centered about this value of $U^\star$ and is instead shifted to higher values, as usually observed (Williamson and Govardhan, 2004). The ratio between the maximum and RMS values of the displacement may depart from $\sqrt{2}$, which reflects a deviation from strictly sinusoidal oscillation. The regularity/modulation of the vibration in the different conditions is specifically addressed in §4.2.

In spite of the possible modulations mentioned above, the structural response is generally dominated by a single frequency, f_ζ, whose evolution with $U^\star$ is depicted in figure 5(c). To ease visualization, the interval of $U^\star$ where the maximum displacement is larger than an arbitrary threshold set to 1% of D, $U^\star \in [4.96, 5.94]$, is indicated by a light blue background color in this plot. As shown by the ratio f_ζ/f_n (left axis), the vibration frequency remains close to the natural frequency of the oscillator, with a slight deviation towards lower values in the largest vibration region. A ratio close to 1 is expected for large $m^\star$ as the influence of the added mass, associated with the fluid force in phase with body acceleration, is marginal (e.g. Sarpkaya, 2004). The value of f_ζ, non-dimensionalized by D and U_∞ is also represented (right axis) for comparison with the Strouhal frequency measured in the fixed body case in §3. The non-dimensional vibration frequencies at the lower and upper edges of the colored region ($\max(\zeta)/D > 1\%$) deviate by +3% and −13% from St, respectively.

The amplitudes reported in prior studies concerning comparable systems are plotted in figure 5(a,b). The selected data sets correspond to configurations with large values of the mass-damping ratio product, where the cylinder spans the width or height of the test section and is exposed to a laminar current. The main characteristics of the systems examined in these previous works are gathered in table 2 and the present system properties are also recalled. The Reynolds number and vibration amplitudes indicated in the table are the peak amplitude values, denoted by the superscript $^{\mathrm{peak}}$. The magnitudes of the structural responses and their global evolutions with $U^\star$ are comparable in all cases. The present results are particularly close to those reported by Feng (1968), which concern a configuration that is the nearest from the present one in terms of Re and $m^\star\xi$ values. The VIV observed by Pastò (2008) occur at lower $U^\star$ values, in accordance with the higher Strouhal frequency identified in this prior study, 0.207 versus 0.194 here; the bell-shaped curves tend to collapse when the amplitude is visualized as a function of $U^\star\mathrm{St}$ (not shown). The vibration frequencies measured by Feng (1968) are plotted in figure 5(c). They exhibit larger departures from f_n, which may relate to the lower value of $m^\star$. The frequency ratio remains however very close to one, as in the present case.

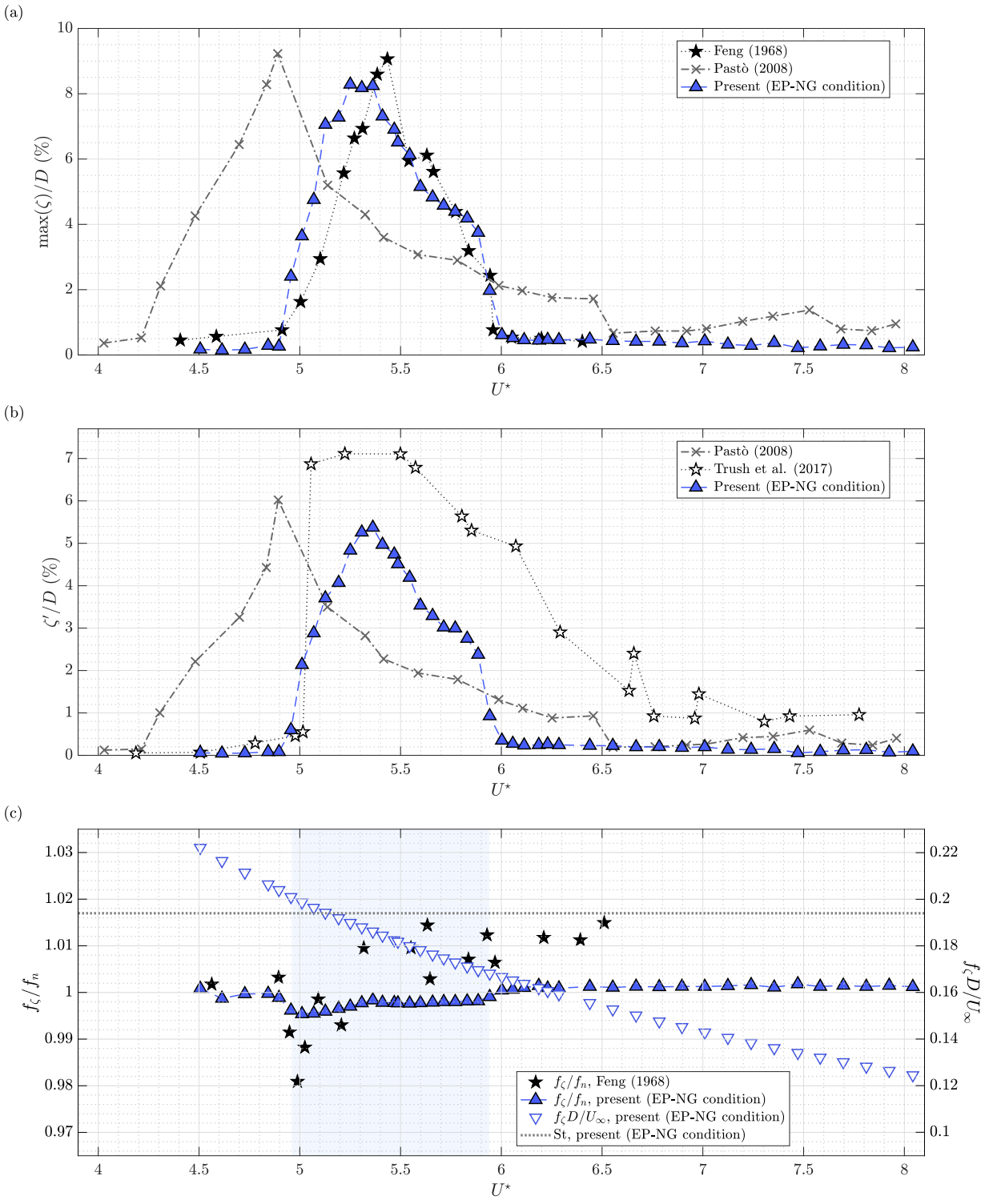

Figure 5: (a) Maximum value, (b) RMS value and (c) dominant frequency of the cylinder displacement as functions of the reduced velocity. In (a,b), the displacement amplitudes are non-dimensionalized by the body diameter. In (c), the vibration frequency is either non-dimensionalized by the natural frequency (left axis) or by the body diameter and freestream velocity (right axis). The Strouhal frequency is that determined in §3 in the EP-NG condition (St = 0.194). The light blue area denotes the region where $\max(\zeta)/D > 1\%$. The present results obtained in the EP-NG condition are compared to data reported by Feng (1968), Pastò (2008) and Trush et al. (2017). The main characteristics of the systems considered in these prior works are summarized in table 2.

Table 2: Some properties of the physical systems and measured vibrations in previous experimental studies concerning cylinder VIV at high mass-damping ratio product in laminar flow. In these prior works, the cylinder spans the height/width of the test section, i.e. there is no free end. The Reynolds number and vibration amplitudes correspond to the peak amplitude values (superscript $^{\text{peak}}$). The present system properties and results (EP-NG condition) are indicated in the last row. The vibration amplitudes are visualized in figure 5(a,b).

Study	L/D	$m^\star$	$m^\star\xi$	$[\text{Re}]^{\text{peak}}$ (10^3)	St	$[\max(\zeta)]^{\text{peak}}/D$ (%)	$[\zeta']^{\text{peak}}/D$ (%)
Feng (1968)	9	248	0.80	18	0.198	9.06	–
Pastò (2008)	15	134	0.67	35	0.207	9.23	6.02
Trush et al. (2017)	4	130	0.58	90	0.2	–	7.11
Present, EP-NG	5.5	875	0.96	11	0.194	8.29	5.37

The proximity of the present system behavior, in the reference condition, with those reported in previous works, confirms the validity of the experimental setup. In the following, it is employed to investigate the influence of the different end and inflow conditions on cylinder VIV.

4.2. Impact of end and inflow conditions

The amplitude of the structural response in the nine end/inflow conditions is visualized in figure 6, via the average of the top 10% of the displacement peaks non-dimensionalized by D. Each panel depicts, for a given inflow condition, the evolution of the amplitude with $U^\star$ for the three end conditions. Substantial vibrations, characterized by bell-shaped evolutions, develop in all cases but an overview of this figure reveals a major impact of the different conditions on the responses, both in terms of magnitude and location along the $U^\star$ range.

Focusing first on the NG condition (figure 6(a)), it appears that the presence of the free end (FF and FH conditions) causes a shift of the bell-shaped curve towards higher $U^\star$ values, compared to the EP condition. This trend, previously detected by Morse et al. (2008) at low $m^\star\xi$, was expected considering the reduction of the Strouhal frequency induced by the free end in the fixed body case (§3). As in the EP condition, the bell-shaped curves are not centered about $U^\star = 1/\text{St}$ (solid vertical lines) in FF and FH conditions, but they occur at lower $U^\star$ values instead of higher ones. In other words, the shift between the response curves is smaller than predicted based on St values. The shift is however such that there is no overlap between the vibration domains in the EP and free-end conditions. The translation along the $U^\star$ range reported by Morse et al. (2008) is comparable to the present one, of the order of 1, but less visible as it involves much wider bell-shaped curves (due to low $m^\star\xi$), which remain mainly superimposed. The peak amplitude, close to 8% of D in the EP condition, decreases in the free-end conditions, down to 6.5% and 4% of D in the FF and FH conditions, respectively. The difference observed between the response magnitude in the two free-end conditions was not expected on the basis of the fixed body case results; in particular, the intensity levels of wake unsteadiness were found to be similar (figure 3(b,c)). A possible explanation could relate to the frontal area exposed to fluid forcing, which is slightly larger in the FF condition ($5.5D^2$) than in the FH condition ($(5 + \pi/8)D^2$). In order to clarify this point, additional experiments have been carried out in the FF condition with a shorter cylinder of aspect ratio $L/D = 5$ (i.e. an exposed area of $5D^2$). The vibration amplitudes (open symbols) are slightly smaller than those measured with the longer body in the FF condition, but clearly larger than in the FH condition. As a result, the alteration of the response magnitude between the FF and FH conditions can be rigorously attributed to the shape of the end.

When the cylinder is placed in a turbulent stream, in the G1 condition (figure 6(b)), the translation of the bell-shaped curve under the effect of the free end appears to be attenuated compared to the laminar inflow condition. Such an attenuation was conjectured based on the closer proximity between the St values in the turbulent inflow conditions (figure 4); the corresponding reduced velocity values, $U^\star = 1/\text{St}$, are represented by solid vertical lines, as in the previous plot. The EP and free-end condition vibration domains slightly overlap. A moderate but persistent enhancement of vibration peak amplitude can be noted in all end conditions. As in laminar flow, the response magnitudes are smaller in the free-end conditions than in the EP condition, and the difference observed between the amplitudes in the FF and FH conditions is found to persist. The actual role played by the hemispherical end shape (versus modification of exposed area) is verified by the results obtained with a shorter cylinder in the FF condition (open symbols).

The trends identified above in the G1 condition are confirmed and amplified in the G2 condition: the overlap between the bell-shaped curves associated with the EP and free-end conditions tends to increase, and vibration magnitudes are further enhanced. The peak amplitudes are close to 12%, 7% and 5% of D, in the EP, FF and FH conditions,

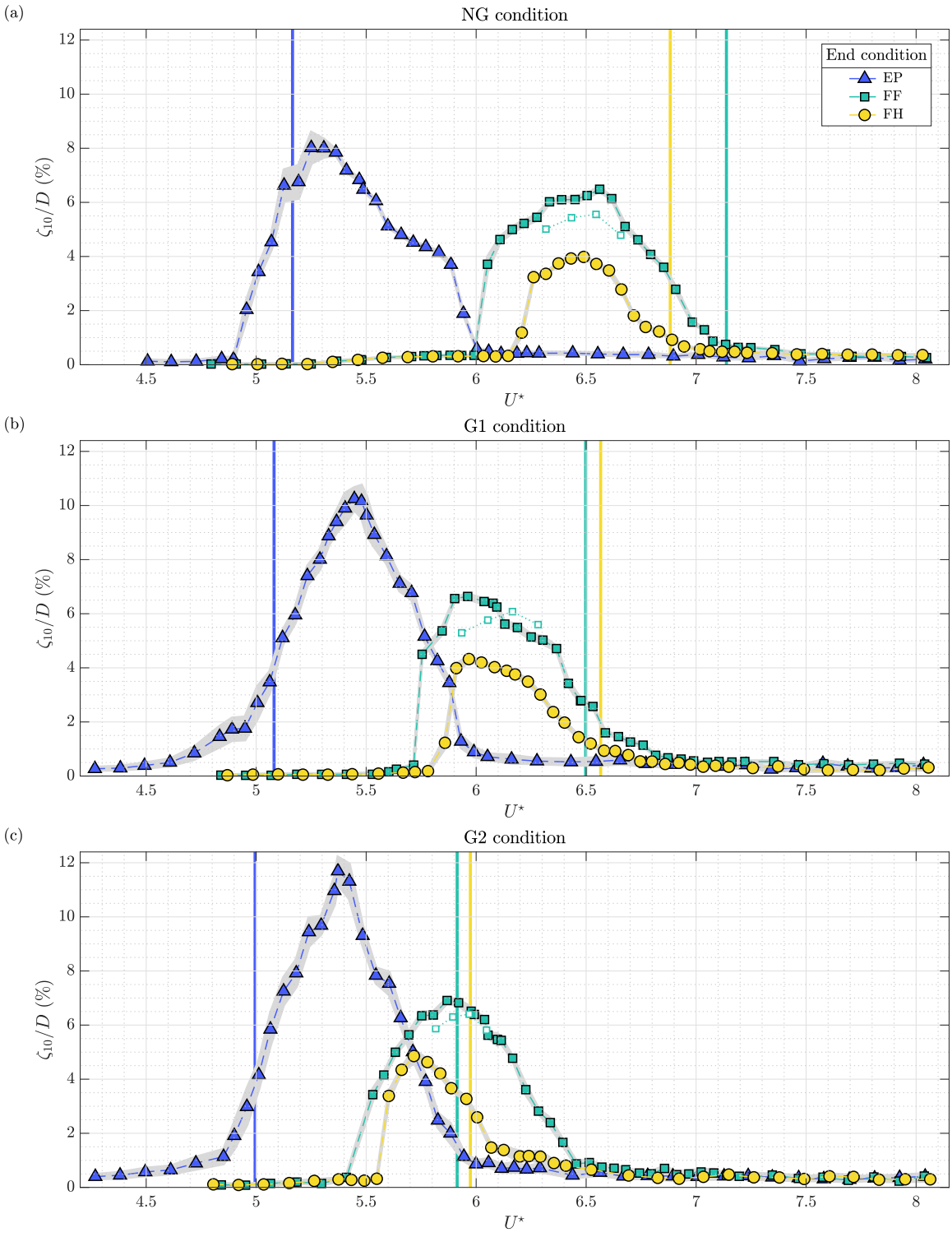

Figure 6: Vibration amplitude as a function of the reduced velocity in the (a) NG, (b) G1 and (c) G2 inflow conditions, for each end condition. The amplitude is quantified via the average of the top 10% of the displacement peaks, non-dimensionalized by the body diameter. The shaded areas depict the RMS values of the displacement envelope fluctuation. Solid vertical lines denote the inverses of the Strouhal frequencies identified in §3 (figure 4), with the same color code as the end conditions in the legend. Additional results for a shorter cylinder ($5D$) in the FF condition are represented by open symbols.

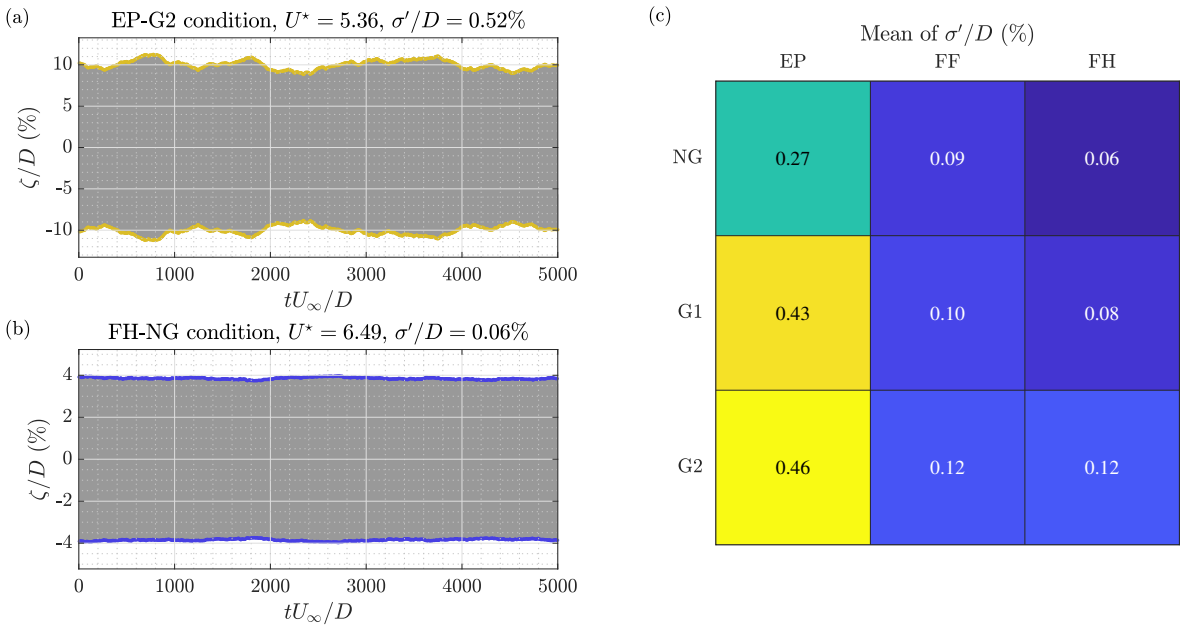

Figure 7: (a,b) Time series of the cylinder displacement, non-dimensionalized by its diameter, in the (a) EP-G2 ($U^\star = 5.36$) and (b) FH-NG ($U^\star = 6.49$) conditions. The time variable is non-dimensionalized by the body diameter and freestream velocity. (c) Mean of the RMS value of the displacement envelope fluctuation, non-dimensionalized by the body diameter, in all end/inflow conditions. The statistics is based on the cases where $\zeta_{10}/D > 1\%$. The color code employed to visualize response regularity ranges from blue to yellow; this color code is used to highlight response envelopes in (a,b).

respectively. The amplification of the peak value relative to the laminar stream condition is particularly notable in the EP condition, +45%, and more temperate in the free-end conditions, +7% (FF) and +22% (FH).

As illustrated in figure 7(a,b) by selected time series of the cylinder displacement, the regularity of the response may substantially vary within the parameter space investigated. The vibration regularity is measured via the RMS value of the displacement envelope fluctuation (σ'), non-dimensionalized by D, which is visualized by shaded areas in figure 6. Low/high σ' values denote regular/irregular responses. In a given condition, some variations may be noted across the $U^\star$ range. For example, in the EP-NG condition and to a lesser extent in the EP-G1 and EP-G2 conditions, response modulations appear to be more pronounced on the left-hand side of the bell-shaped curve than on the right-hand side. General features can however be identified among the different end/inflow conditions, by considering the mean value of σ'. This statistics based on all cases where $\zeta_{10}/D > 1\%$ and non-dimensionalized by D, is presented, for each condition, in figure 7(c). The vibrations are found to be less regular in the EP condition than in the free-end conditions. Such a trend may seem rather counter-intuitive in view of the richer frequency content of the fixed body wake in the latter conditions (figure 4). It can be observed qualitatively in the time series reported by Morse et al. (2008), in laminar flow, for cases with and without end plates (figure 5 in this previous paper). The present results show that this effect of the end condition on vibration regularity persists regardless of the inflow condition. On the other hand, a second trend emerges from figure 7(c): turbulent freestreams tend to enhance the modulations of the structural responses and lead to higher irregularity levels, especially in the EP condition. The examples selected in figure 7(a,b), i.e. typical cases of the EP-G2 and FH-NG conditions, thus depict the extreme behaviors encountered in the present work, in terms of response regularity.

In order to examine the coupling mechanism between the elastically mounted body and the flow, the evolution of the frequency content of the wake with $U^\star$ is represented in figure 8, together with the vibration frequency (black dot), in the nine end/inflow conditions. For each reduced velocity, the spectral amplitude is normalized by its peak value and the frequencies are non-dimensionalized by f_n. It is recalled that the spectra used to quantify wake unsteadiness are based on time series of flow velocity sampled downstream of the cylinder, at $1.5D$ from its base; the evolution of flow velocity spectrum along the span is discussed later in this subsection. To facilitate the combined analysis of the wake and body responses, the vibration amplitude is also plotted in each panel (right axis).

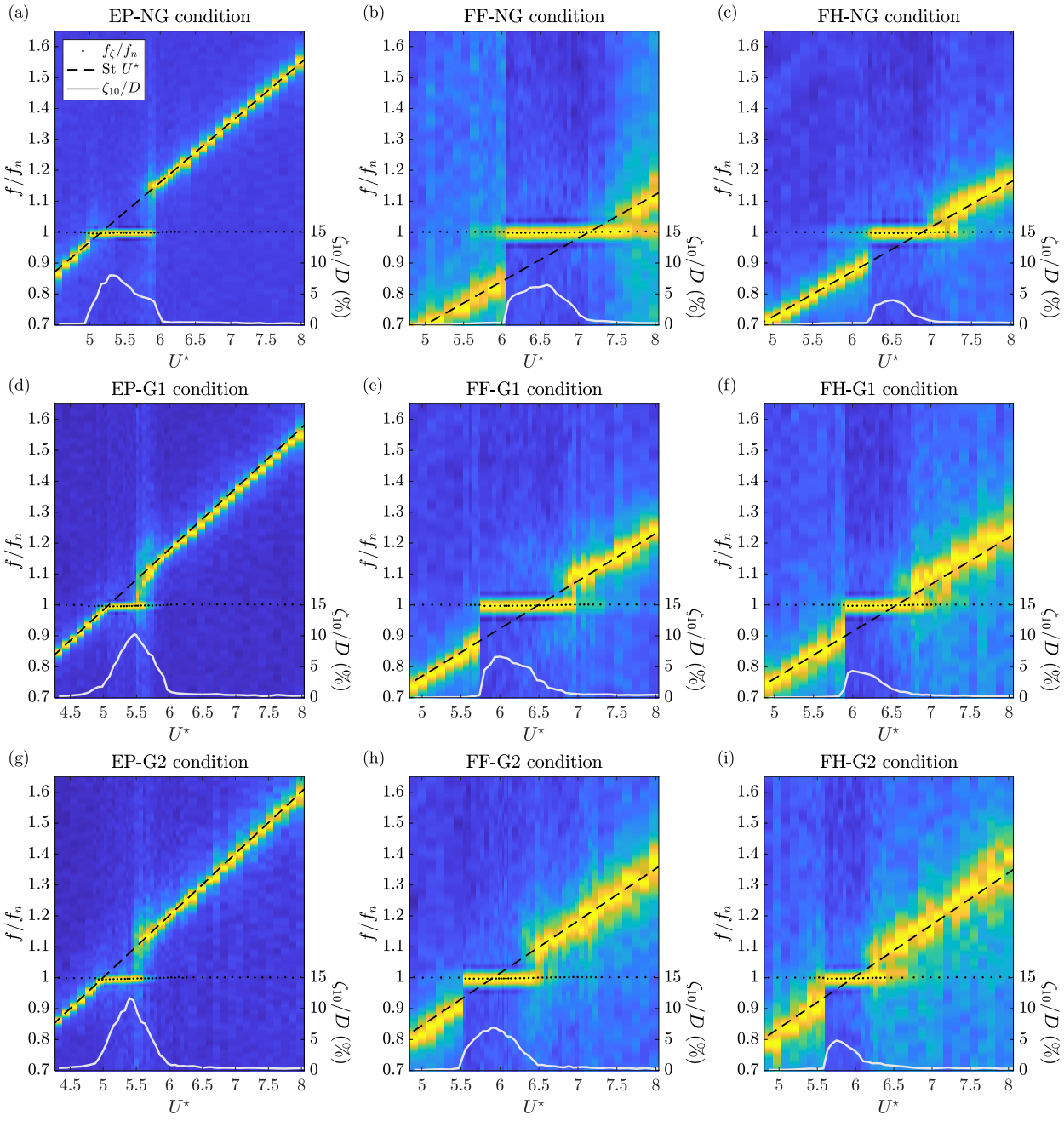

Figure 8: Frequency spectrum of flow velocity fluctuation in the wake of the elastically mounted cylinder ($1.5D$ from the base, $3.5D$ downstream and $0.75D$ aside from the centerline), as a function of the reduced velocity, in the (a) EP-NG, (b) FF-NG, (c) FH-NG, (d) EP-G1, (e) FF-G1, (f) FH-G1, (g) EP-G2, (h) FF-G2 and (i) FH-G2 conditions. The spectral amplitude is normalized by its maximum value for each reduced velocity and the color levels range from 0 (blue) to 1 (yellow). The frequency range is non-dimensionalized by the natural frequency of the oscillator. A black dot denotes the vibration frequency for each $U^\star$ value. A black dashed line represents the Strouhal frequency identified in figure 4 (fixed body). The vibration amplitude is recalled at the bottom of each panel (ζ_{10}/D; gray solid line, right axis).

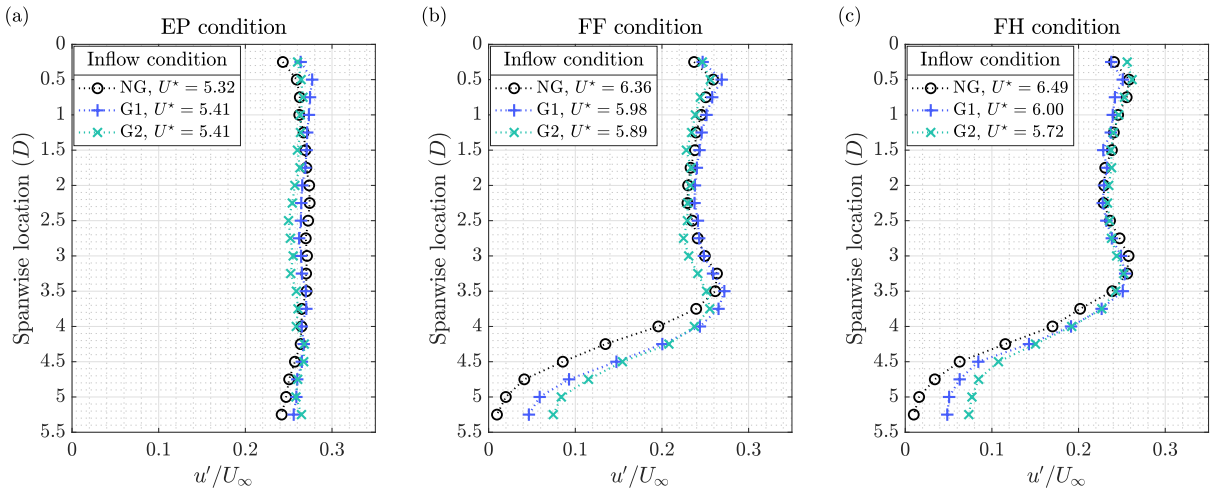

Figure 9: Same as figure 3 in the wake of the elastically mounted cylinder, close to vibration peaks. The values of the reduced velocity are specified in the legends.

As previously observed in the EP-NG condition (figure 5(c)), the vibration frequency remains very close to f_n throughout the $U^\star$ range in all conditions, as expected for large $m^\star$. It only deviates towards slightly lower values in the region where the largest responses develop. The emergence of significant vibrations involves a synchronization of flow unsteadiness and body motion, the lock-in phenomenon, which is characterized by the coincidence of wake and vibration frequencies. The occurrence of lock-in is associated, in the wake, with a depature from the Strouhal frequency identified downstream of the fixed body (black dashed line; St values are indicated in figure 4). The negative relative deviations from St are comparable in all conditions, around -10%. The positive deviations appear to be larger in the free-end conditions, up to $+20\%$, than in the EP condition. No specific trend arises regarding the influence of the inflow condition. At the edges of the lock-in range, incommensurable spectral components at the vibration frequency (thus close to f_n) and Strouhal frequency may coexist, and simultaneously contribute to flow unsteadiness.

As a complementary observation, the proximity between the Strouhal frequency measured at $U_\infty = 3$ m/s (black dashed line), i.e. $\mathrm{Re} = 12 \times 10^3$, and the frequency of flow unsteadiness out of the lock-in region, indicates that St is close to constant over the Reynolds number range under study, $\mathrm{Re} \in [9 \times 10^3, 17 \times 10^3]$.

To further analyze the alteration of the flow once VIV develop, the intensity of its unsteadiness along the span, downstream of the vibrating body, is visualized in figure 9. A case close to the peak of vibration amplitude is considered for each condition; the corresponding $U^\star$ values are indicated in the legends. The levels and spatial distributions of flow unsteadiness intensity are globally comparable to those measured in the wake of the fixed cylinder (figure 3). Yet, some differences can be noted. For each end condition, VIV are accompanied by an homogenization of the profiles between the three inflow conditions. This is particularly visible in the free-end conditions, where the drop of fluctuation intensity occurs at similar spanwise locations regardless of the inflow condition. It can also be observed that the intensity drop tends to occur closer to the tip once the body vibrates, for example, in the FF-NG condition, beyond $3.5D$ from the base versus $2.75D$ in the fixed body case. The displacement of the drop towards the tip, and the associated expansion of the plateau of high fluctuation intensity, appear to be more pronounced in the FF condition than in the FH condition. This phenomenon may be connected to vibration amplitudes, which are substantially larger in the former condition. It is recalled that no clear effect of the free-end shape on flow unsteadiness intensity was detected downstream of the fixed cylinder.

The spanwise evolution of flow frequency content is represented in figure 10, for the nine VIV cases examined in figure 9. A sharp peak at the vibration frequency (gray dashed-dotted line) dominates flow velocity spectrum over the entire span in the EP condition and over most of the span in the free-end conditions. In the FF and FH conditions, in spite of some lower-frequency components, the presence of this peak can still be discerned in the region perturbed by the free end, i.e. the region of intensity drop in figure 9. The trace of the lock-in phenomenon is thus found to persist along the entire cylinder. This contrasts with the fixed body wakes, where the trace of the spectral component

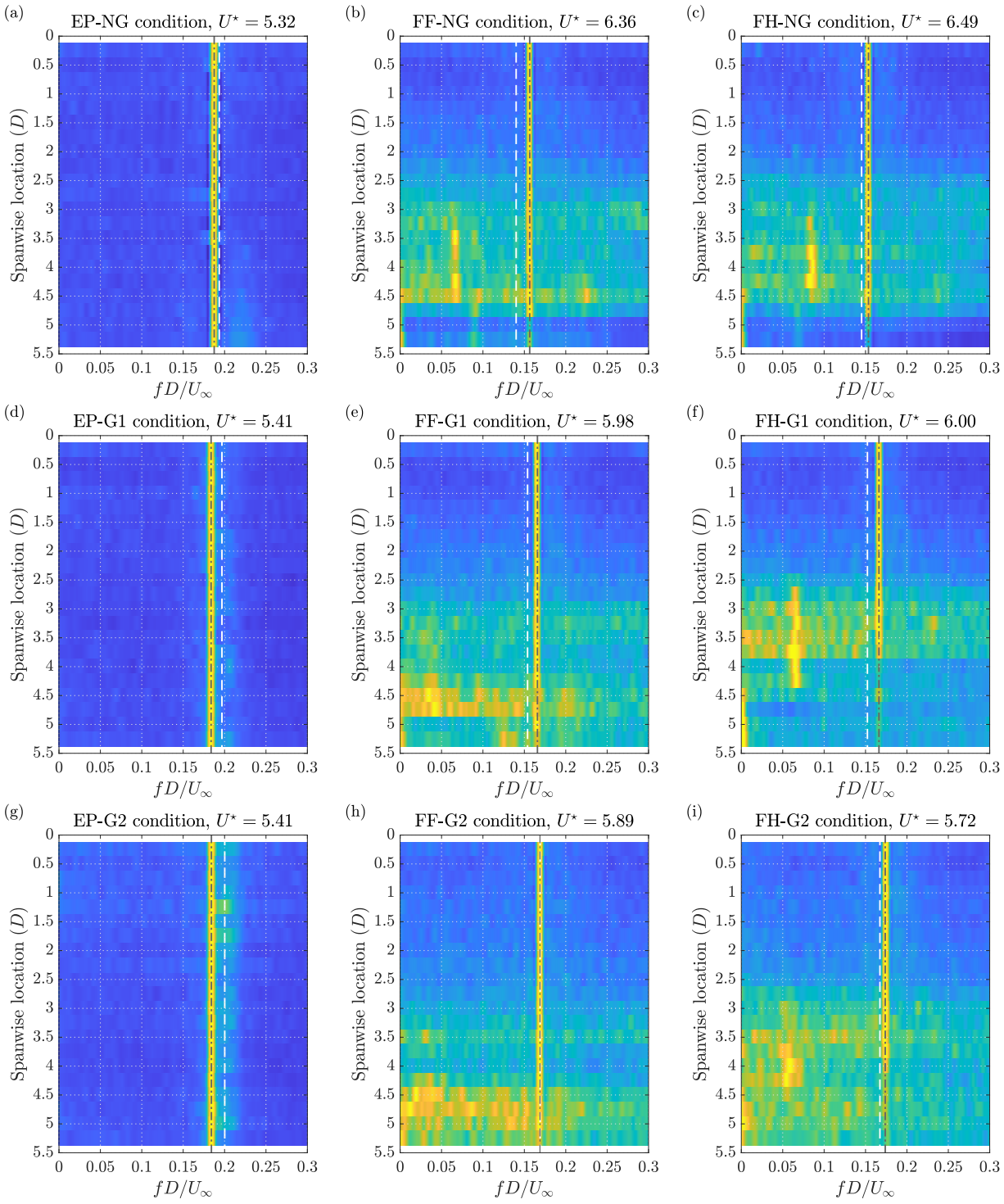

Figure 10: Same as figure 4 in the wake of the elastically mounted cylinder, close to vibration peaks. The reduced velocity values are the same as in figure 9; they are specified above each panel. A white dashed line indicates the Strouhal frequency identified in figure 4 (fixed body) while a gray, dashed-dotted line denotes the vibration frequency.

dominating flow unsteadiness in the upper part of the wake, close to the cylinder base, is lost in the free-end region (figure 4). The spectra plotted in figure 10 also provide a complementary vision of the departure from the Strouhal frequency, which is indicated by a white dashed line in each panel.

5. Conclusions

The impact of end and inflow conditions on the vortex-induced vibrations of a cylinder has been investigated on the basis of wind tunnel experiments, combining measurements of the body displacement and flow velocity in the wake. The study was carried out for a cylinder of a length-to-diameter aspect ratio equal to 5.5, with one end exposed to the current. The body of mass ratio close to 1000 was elastically mounted in the cross-flow direction, with low structural damping. The behavior of the flow-structure system was explored over a range of reduced velocity values, roughly between 4 and 8, at a Reynolds number of the order of 10^4. Three end conditions have been examined: two free-end conditions with either a flat or a hemispherical shape, and a condition where a fixed plate was placed close to the flat end. The influence of the end condition has been analyzed for three inflow conditions: a laminar condition, obtained by considering the empty wind tunnel, and two turbulent conditions, achieved by placing grids at the inlet of the test section. The levels of turbulence intensity in the latter two conditions were close to 6% and 10%, with comparable integral length scales, around 30% of the cylinder diameter.

Vibrations characterized by bell-shaped evolutions of their amplitude with $U^\star$ develop in the nine end/inflow conditions investigated. They occur under lock-in, i.e. the mechanism of flow-body synchronization typical of VIV. Their frequency may deviate from the Strouhal frequency measured downstream of the fixed cylinder but remains close to the natural frequency of the oscillator, as expected for large mass ratios. The structural responses observed in the reference condition (end plate and laminar inflow) are comparable to those reported in prior works concerning similar systems, with a peak amplitude close to 8% of the body diameter.

The most prominent effects of the end condition, which persist regardless of the inflow condition, can be summarized as follows.

- The free end causes a shift of the response bell-shaped curve towards higher $U^\star$ values. This phenomenon was predicted, actually overestimated, based on the reduction of the Strouhal frequency induced by the free end, for example from 0.194 to 0.14 in the laminar inflow condition. The shift may be large enough to suppress the overlap between the vibration domains in the end-plate and free-end conditions.
- A reduction of vibration amplitude is observed when the end plate is removed, from 8% to 6.5% of D for the peak amplitudes in the laminar inflow condition. The response magnitude is further reduced when the flat end is replaced by the hemispherical one, with a peak amplitude close to 4% of D.
- The vibrations are found to be more regular in the free-end conditions than in the end-plate condition. The stronger modulations of the response envelope in the latter condition may appear relatively counter-intuitive in view of the richer frequency content measured in the wake of the fixed body with a free end.

This work also highlights the impact of the inflow condition on the system behavior. The following trends have been uncovered.

- The translation of the bell-shaped curve of response amplitude along the $U^\star$ range, under the influence of the free end, is attenuated by the passage from laminar to turbulent inflow conditions. This results in an overlap of the vibration domains in the end-plate and free-end conditions.
- Turbulent inflows induce an amplification of the vibrations. This enhancement relative to the laminar flow condition is particularly notable with the end plate, +45% for the peak amplitude.
- The inflow condition is found to influence the regularity of the structural responses and it is shown that turbulent freestreams tend to trigger vibration modulations.
- The three effects of turbulent inflows described above are strengthened as the level of turbulence intensity is increased.

Acknowledgments

The authors gratefully acknowledge the technical support of Jean-Dominique Barron and Christophe Korbuly from the *IXP Service* at IMFT.

References

Azadeh-Ranjbar, V., Elvin, N., Andreopoulos, Y., 2018. Vortex-induced vibration of finite-length circular cylinders with spanwise free-ends: Broadening the lock-in envelope. Physics of Fluids 30, 105104.

Basu, R.I., 1986. Aerodynamic forces on structures of circular cross-section. Part 2. The influence of turbulence and three-dimensional effects. Journal of Wind Engineering and Industrial Aerodynamics 24, 33–59.

Bearman, P.W., Morel, T., 1983. Effect of free stream turbulence on the flow around bluff bodies. Progress in Aerospace Sciences 20, 97–123.

Blackburn, H.M., Melbourne, W.H., 1996. The effect of free-stream turbulence on sectional lift forces on a circular cylinder. Journal of Fluid Mechanics 306, 267–292.

Cardesa, J.I., Nickels, T.B., Dawson, J.R., 2012. 2D PIV measurements in the near field of grid turbulence using stitched fields from multiple cameras. Experiments in Fluids 52, 1611–1627.

Dogan, E., Hanson, R.E., Ganapathisubramani, B., 2016. Interactions of large-scale free-stream turbulence with turbulent boundary layers. Journal of Fluid Mechanics 802, 79–107.

Dyrbye, C., Hansen, S.O., 1997. Wind load on structures. Wiley, Chichester.

Farivar, D., 1981. Turbulent uniform flow around cylinders of finite length. AIAA Journal 19, 275–281.

Feng, C.C., 1968. The measurement of vortex-induced effects in flow past stationary and oscillating circular and D-section cylinders. Master's thesis, Univ. British Columbia .

Fox, T.A., Apelt, C.J., 1993. Fluid-induced loading of cantilevered circular cylinders in a low-turbulence uniform flow. Part 3: Fluctuating loads with aspect ratios 4 to 25. Journal of Fluids and Structures 7, 375–386.

Gerich, D., Eckelmann, H., 1982. Influence of end plates and free ends on the shedding frequency of circular cylinders. Journal of Fluid Mechanics 122, 109–121.

Gonçalves, R.T., Meneghini, J.R., Fujarra, A.L.C., 2018a. Vortex-induced vibration of floating circular cylinders with very low aspect ratio. Ocean Engineering 154, 234–251.

Gonçalves, R.T., Sakata, K., Gambarine, D.M., Cicolin, M.M., Hirabayashi, S., Assi, G.R.S., 2018b. Experimental study on vortex-induced vibration of floating circular cylinders with low aspect ratio and different free-end corner shapes. Proceedings of the ASME 37th International Conference on Ocean, Offshore and Arctic Engineering , OMAE2018–77218.

Govardhan, R., Williamson, C.H.K., 2006. Defining the 'modified Griffin plot' in vortex-induced vibration: revealing the effect of Reynolds number using controlled damping. Journal of Fluid Mechanics 561, 147–180.

Hajimirzaie, S.M., Wojcik, C.J., Buchholz, J.H.J., 2012. The role of shape and relative submergence on the structure of wakes of low-aspect-ratio wall-mounted bodies. Experiments in Fluids 53, 1943–1962.

Hover, F.S., Techet, A.H., Triantafyllou, M.S., 1998. Forces on oscillating uniform and tapered cylinders in crossflow. Journal of Fluid Mechanics 363, 97–114.

Inoue, O., Sakuragi, A., 2008. Vortex shedding from a circular cylinder of finite length at low Reynolds numbers. Physics of Fluids 20, 033601.

Iungo, G.V., Pi, L.M., Buresti, G., 2012. Experimental investigation on the aerodynamic loads and wake flow features of a low aspect-ratio circular cylinder. Journal of Fluids and Structures 28, 279–291.

Kareem, A., Cheng, C.M., Lu, P.C., 1989. Pressure and force fluctuations on isolated circular cylinders of finite height in boundary layer flows. Journal of Fluids and Structures 3, 481–508.

Kawamura, T., Hiwada, M., Hibino, T., Mabuchi, I., Kumada, M., 1984. Flow around a finite circular cylinder on a flat plate : Cylinder height greater than turbulent boundary layer thickness. Bulletin of Japan Society of Mechanical Engineers 27, 2142–2151.

Khalak, A., Williamson, C.H.K., 1996. Dynamics of a hydroelastic cylinder with very low mass and damping. Journal of Fluids and Structures 10, 455–472.

Kitagawa, T., Fujino, Y., Kimura, K., Mizuno, Y., 2002. Wind pressures measurement on end-cell-induced vibration of a cantilevered circular cylinder. Journal of Wind Engineering and Industrial Aerodynamics 90, 395–405.

Klamo, J.T., Leonard, A., Roshko, A., 2006. The effects of damping on the amplitude and frequency response of a freely vibrating cylinder in cross-flow. Journal of Fluids and Structures 22, 845–856.

Konstantinidis, E., Zhao, J., Leontini, J., Jacono, D.L., Sheridan, J., 2020. Phase dynamics of effective drag and lift components in vortex-induced vibration at low mass–damping. Journal of Fluids and Structures 96, 103028.

Leontini, J.S., Thompson, M.C., Hourigan, K., 2006. The beginning of branching behaviour of vortex-induced vibration during two-dimensional flow. Journal of Fluids and Structures 22, 857–864.

Mittal, S., Tezduyar, T.E., 1992. A finite element study of incompressible flows past oscillating cylinders and aerofoils. International Journal for Numerical Methods in Fluids 15, 1073–1118.

Morse, T.L., Govardhan, R.N., Williamson, C.H.K., 2008. The effect of end conditions on the vortex-induced vibration of cylinders. Journal of Fluids and Structures 24, 1227–1239.

Norberg, C., 1994. An experimental investigation of the flow around a circular cylinder: influence of aspect ratio. Journal of Fluid Mechanics 258, 287–316.

Païdoussis, M.P., Price, S.J., de Langre, E., 2010. Fluid-Structure Interactions: Cross-Flow-Induced Instabilities. Cambridge University Press.

Park, C.W., Lee, S.J., 2000. Free end effects on the near wake flow structure behind a finite circular cylinder. Journal of Wind Engineering and Industrial Aerodynamics 88, 231–246.

Park, C.W., Lee, S.J., 2004. Effects of free-end corner shape on flow structure around a finite cylinder. Journal of Fluids and Structures 19, 141–158.

Pastò, S., 2008. Vortex-induced vibrations of a circular cylinder in laminar and turbulent flows. Journal of Fluids and Structures 24, 977–993.

Porteous, R., Moreau, D.J., Doolan, C.J., 2014. A review of flow-induced noise from finite wall-mounted cylinders. Journal of Fluids and Structures 51, 240–254.

Prasanth, T.K., Premchandran, V., Mittal, S., 2011. Hysteresis in vortex-induced vibrations: critical blockage and effect of m^*. Journal of Fluid Mechanics 671, 207–225.

Raghavan, K., Bernitsas, M.M., 2011. Experimental investigation of Reynolds number effect on vortex-induced vibration of rigid circular cylinder on elastic supports. Ocean Engineering 38, 719–731.
Rahman, M.A.A., Thiagarajan, K.P., 2015. Experiments on vortex-induced vibration of a vertical cylindrical structure: effect of low aspect ratio. International Journal of Automotive and Mechanical Engineering 11, 2515–2530.
Riches, G., Morton, C., 2018. One degree-of-freedom vortex-induced vibrations at constant Reynolds number and mass-damping. Experiments in Fluids 59, 157.
Roach, P.E., 1987. The generation of nearly isotropic turbulence by means of grids. International Journal of Heat and Fluid Flow 8, 82–92.
Sarpkaya, T., 2004. A critical review of the intrinsic nature of vortex-induced vibrations. Journal of Fluids and Structures 19, 389–447.
Schouveiler, L., Provansal, M., 2001. Periodic wakes of low aspect ratio cylinders with free hemispherical ends. Journal of Fluids and Structures 15, 565–573.
Shiels, D., Leonard, A., Roshko, A., 2001. Flow-induced vibration of a circular cylinder at limiting structural parameters. Journal of Fluids and Structures 15, 3–21.
Slaouti, A., Gerrard, J.H., 1981. An experimental investigation of the end effects on the wake of a circular cylinder towed through water at low reynolds numbers. Journal of Fluid Mechanics 112, 297–314.
So, R.M.C., Wang, X.Q., Xie, W.C., Zhu, J., 2008. Free-stream turbulence effects on vortex-induced vibration and flow-induced force of an elastic cylinder. Journal of Fluids and Structures 24, 481–495.
Sumner, D., 2013. Flow above the free end of a surface-mounted finite-height circular cylinder: A review. Journal of Fluids and Structures 43, 41–63.
Surry, D., 1972. Some effects of intense turbulence on the aerodynamics of a circular cylinder at subcritical Reynolds number. Journal of Fluid Mechanics 52, 543–563.
Trush, A., Pospíšil, S., Kozmar, H., 2020. Comparison of turbulence integral length scale determination methods. WIT Transactions on Engineering Sciences, Advances in Fluid Mechanics XIII 128, 113–123.
Trush, A., Pospíšil, S., Kuznetsov, S., Kozmar, H., 2017. Wind-tunnel experiments on vortex-induced vibration of rough bridge cables. Journal of Bridge Engineering 22, 06017001.
Williamson, C.H.K., Govardhan, R., 2004. Vortex-induced vibrations. Annual Review of Fluid Mechanics 36, 413–455.
Zdravkovich, M.M., Brand, V.P., Mathew, G., Weston, A., 1989. Flow past short circular cylinders with two free ends. Journal of Fluid Mechanics 203, 557–575.
Zhao, M., Cheng, L., 2014. Vortex-induced vibration of a circular cylinder of finite length. Physics of Fluids 26, 015111.